PAPER

Check for updates

Oxygen vacancy engineering and redox coupling-driven enhancement of extended wavelength light absorption and energy storage in Ca(OH)$_2$–Sr$_{0.4}$Co$_{2.6}$O$_4$ *via* photothermal dehydration

Lin Zhu,[a] Rui-Min Hao,[a] Ti-Jian Du,[b] Cheng-Hui Liu,[c] Zhi-Bin Xu[a] and Qin-Pei Wu [iD] *[a]

Photothermal efficiency is predominantly governed by efficient near-infrared (NIR) light harvesting through surface plasmon resonance (SPR) absorption mechanisms. However, current methodologies for achieving robust absorption of long-wavelength radiation remain fundamentally limited. Herein, we pioneer the synergistic interplay between oxygen vacancies and redox activity as a novel strategy to substantially enhance free-carrier concentration, contract bandgaps, improve NIR light absorption capabilities, elevate photothermal temperatures, and intensify photocurrent. Through strategic substitution of Co^{2+} with larger Sr^{2+} ions within the Co$_3$O$_4$ lattice, we synthesize Sr$_{0.4}$Co$_{2.6}$O$_4$ nanoparticles exhibiting exceptional oxygen vacancy concentrations (52%), which simultaneously activate abundant redox reactions and exhibit 1.63-fold enhancement in absorption efficiency across vis-NIR light. This material achieves an extraordinarily high free-carrier density of 1.2×10^{21} cm^{-3}, establishing new fundamental understanding in atomic-level absorber design and oxygen-vacancy-mediated light-harvesting mechanism. Furthermore, this multifunctional material demonstrates substantial photothermal performance enhancement, achieving 4.8-fold improvement in dehydration conversion efficiency, 3.4-fold acceleration of dehydration reaction kinetics, and 37.5-fold increased stability of thermal charge and discharge cycles in Ca(OH)$_2$–Sr$_{0.4}$Co$_{2.6}$O$_4$ systems.

Broader context

Through strategic substitution of Co^{2+} with larger Sr^{2+} ions in the Co$_3$O$_4$ lattice, Sr$_{0.4}$Co$_{2.6}$O$_4$ nanoparticles achieve an ultrahigh oxygen vacancy concentration of 52 at%. The synergistic interaction between oxygen vacancies and redox-active sites significantly increases the free-carrier concentration (1.37×10^{21} cm^{-3}), reduces the bandgap energy ($E_g = 0.35$ eV), enhances near-infrared light absorption ($A = 1.35$), improves photothermal conversion efficiency (86%), and boosts photocurrent generation with a 15.4-fold enhancement.

1. Introduction

Solar energy represents the most abundant and promising renewable energy source on Earth. Near-infrared (NIR) light constitutes approximately 53% of the total solar irradiance, yet its efficient utilization remains a critical challenge. The harvesting of NIR radiation primarily relies on the surface plasmon resonance (SPR) effect, which facilitates the conversion of light energy into thermal energy. Consequently, photothermal conversion emerges as a highly effective strategy for maximizing solar energy capture.[1] Near-infrared (NIR) radiation (780–2500 nm wavelength) exhibits deep tissue penetration capabilities (1.5–2 cm depth), demonstrating significant potential for phototherapeutic applications.[2] This spectral range has been harnessed for multifunctional energy conversion processes including seawater desalination, solar-driven evaporation,[3] catalytic processes,[4] and photothermal imaging diagnostics.[5] Notably, within the full solar spectrum, NIR radiation demonstrates dominant photothermal performance characteristics. Consequently, optimizing NIR light harvesting efficiency constitutes a critical determinant for advanced photothermal material design. The SPR phenomenon is typically induced by a high density of free charge carriers (FCC), exceeding a concentration of 10^{18} cm^{-3}.[6]

Conventional plasmonic nanomaterials, including Au, Ag, Pt, Al, Cu, Co, In, Ni, Ti, and Fe, primarily absorb UV and visible

[a]School of Chemistry and Chemical Engineering, Beijing Institute of Technology, Beijing, 102488, China. E-mail: qpwu@bit.edu.cn

[b]Yantai Valiant Pharmaceutical Co., Ltd, 60 Taiyuan Rd, Dajijia Industrial Park, YEDA, Yantai, Shandong, China

[c]School of Material Science and Engineering, Beijing Institute of Technology, Beijing, 102488, China

light (comprising ~46% of the solar spectrum) while exhibiting poor performance in the NIR region.[7] Additionally, these metallic nanoparticles suffer from limited scalability in large-scale production and exhibit thermal instability under high photothermal temperatures. To address these limitations, lattice-defect engineering—such as introducing cation vacancies and oxygen vacancies (OVs)—has been demonstrated as an effective approach to narrow the bandgap and enable broadband absorption.[8] Notably, cation-deficient materials, such as metallic chalcogenides (*e.g.*, nonstoichiometric $Cu_{2-x}S$ and $Cu_{2-x}Se$ with $E_g = \sim2.0$ eV),[9] exhibit pronounced SPR activity,[10] presenting promising alternatives for efficient solar energy harnessing.

Following $NaBH_4$-mediated hydrogenation, WO_3 ($E_g = 3.4$ eV) undergoes structural transformation into a quasi metallic $WO_{2.9}$ (6.3×10^{21} cm^{-3}) phase containing oxygen vacancies, which enables broadband solar absorption across the entire visible-near infrared spectrum.[11] Similarly, TiO_2 (band gap 3.3 eV) experiences reduction to form Ti_2O_3 with a significantly narrowed bandgap of 0.1 eV, permitting comprehensive light harvesting from 300 nm to 2500 nm wavelengths.[12] However, the fundamental mechanism underlying lattice-defect-mediated light absorption enhancement remains incompletely understood. Our experimental verification demonstrates that interfacial junction architectures substantially enhance FCC concentration while simultaneously reducing bandgap energy for extended absorption into near-infrared regions.[13,14] The CeO_x–Co_3O_4 redox couple exhibits exceptionally high FCC density with full spectrum absorption.[15] Notably, the majority of plasmonic metal oxides predominantly absorb in visible and NIR-I regions (700–1100 nm),[16] leaving a critical gap in near-infrared-II (NIR-II) responsive photothermal materials. Current strategies for achieving full solar spectrum absorption remain highly challenging, underscoring the urgent need for innovative approaches to optimize FCC engineering and expand light absorption into the biological transparency window (NIR-II). Herein, we report that $Sr_{0.4}Co_{2.6}O_4$ nanoparticles exhibit high FCC density and a narrow band gap, attributable to the abundance of OVs. The numerous redox reactions of radicals at these OVs facilitate these properties, providing in-depth insights into the mechanism of defect engineering.

Furthermore, the inherent instability and intermittent nature of solar irradiance present significant challenges to effective utilization of this vast renewable energy resource. Thermal energy storage (TES) technologies emerge as a promising solution to these limitations.[17] Among various TES approaches, thermochemical heat storage (TCHS) systems leverage reversible thermochemical reactions to enable seasonal energy storage across summer–winter cycles, demonstrating exceptional potential for long-term thermal energy management.[13,18–20] The operational efficiency of these TCHS systems critically depends on two key parameters: the reaction conversion efficiency and the kinetic characteristics of the thermochemical processes.[21]

In conventional systems, thermal-energy-storage materials exhibit insufficient light absorption for effective photothermal utilization. Previous studies have demonstrated enhanced light harvesting in $CaCO_3$ matrices through integration with metal-oxide photothermal materials, including $FeMnO_3$–Fe_2O_3 heterostructures,[22] FeO_x/Al_2O_3 composite interfaces,[23] Ce/Co/Mn oxide solid solutions,[24] CuO-based mixed metal oxides (CuO–$CoO_x/CrO_x/FeO_x/MnO_x$),[25] MnO_x/Cr_2O_3 coupled systems,[26] and SiC–MnO_2 composites.[27] Notably, nanocomposite architectures such as Co_3O_4–$Co_3(PO_4)_2$ heterojunctions ($E_g = 0.40$ eV),[13] CrO_x–SiO_2 interfaces ($E_g = 0.24$ eV),[14] and Co_2SiO_4–SiO_2 ($E_g = 0.38$ eV) solid solutions[28] exhibit enhanced solar absorptivity through interfacial charge separation mechanisms, while CeO_x–Co_3O_4 redox systems[15] demonstrate significant photothermal temperature elevation and improved hydroxide phase transition reversibility for integrated solar-driven thermal storage.

This study reveals that $Sr_{0.4}Co_{2.6}O_4$ achieves unprecedented photothermal performance through synergistic interplay between abundant OVs and redox-active cobalt–oxygen clusters. The material's optimized face-centered cubic phase distribution and narrowed bandgap configuration enable comprehensive solar spectrum utilization, achieving 3.2-fold enhancement in light absorption compared to conventional perovskite analogs. Experimental validation demonstrates that $Sr_{0.4}Co_{2.6}O_4$ nanoparticles accelerate $Ca(OH)_2$ dehydration kinetics by 47% under simulated solar irradiation while maintaining excellent cycle stability for 30 hydration–dehydration cycles. The synergistic optimization of OV concentration (52%) and redox-active components yields an innovative framework for advancing high-efficiency solar-thermal energy storage materials. This approach provides a viable pathway to simultaneously enhance light harvesting efficiency and reaction reversibility through coordinated defect engineering and redox coupling strategies.

2. Experimental section

2.1. Chemicals and instruments

Chemicals, $Co(NO_3)_2 \cdot 6H_2O$, $Sr(NO_3)_2$, citric acid, polyethylene glycol (molecular weight 20 000 g mol^{-1}), and glycine, were purchased from Beijing Chemical Co., Ltd, China. These chemicals were recrystallized before use (~99% purity). $Ca(OH)_2$ (97.6%) was prepared with a previous procedure.[19] Thermogravimetric analysis (TG) and differential scanning calorimetry (DSC) were carried out with SDT-Q600 under nitrogen atmosphere. Xe lamp (GME Xe-300F, 300–2500 nm) was employed to simulate solar irradiation. The optical absorption was recorded with a Shimadzu UV-3600 spectrophotometer (200–2500 nm). Pure $BaSO_4$ was used as the reflectance standard material.

The compositions and crystallographic phase of as-prepared materials were identified on an X-ray diffractometer (XRD, Ultima IV) with monochromatized Cu-K$_\alpha$ radiation (0.154059 nm, 40 kV). The XRD patterns were operated in the 2θ range of 10° to 80° at a scanning rate of 2° min^{-1}. Microscopic morphology of the materials was measured by scanning electron microscopy (SEM, ZEISS Gemini SEM 300) and transmission electron microscopy (TEM, JEOL JEM-F200) micrographs. X-ray photoelectron spectroscopy (XPS) spectra were recorded with the Thermo Scientific K-Alpha

photoelectron spectrometer by using an Al K_{α} radiation source (1486.6 eV). The electron paramagnetic resonance (EPR) was performed on a Bruker EMXplus-6/1 spectrometer at 298 K with 4.00 G modulation amplitude and a magnetic field modulation of 100 kHz.

2.2. General procedure for preparation of $M_xCo_{3-x}O_4$

General procedure for preparation of $M_xCo_{3-x}O_4$ (M = Sr^{2+}, Cu^{2+}, Ca^{2+}, and Zn^{2+}): Citric acid (1.8 g) was dissolved in deionized water (5 mL) and followed by adding $Co(NO_3)_2 \cdot 6H_2O$ (1.46 g, 5 mmol) and $Sr(NO_3)_2$ (0.16 g, 0.75 mmol) or $Cu(NO_3)_2 \cdot 3H_2O$ (0.14 g, 0.75 mmol). This solution was stirred at 80 °C to be a gel, which was sequentially maintained at 280 °C for 4 h, and 650 °C for 4 h at heating rate of 8 °C min^{-1} under air to form the desired $Sr_{0.4}Co_{2.6}O_4$ or $Cu_{0.4}Co_{2.6}O_4$ nano particles (Fig. S1).

2.3. Preparation of $Ca(OH)_2$–15 wt% $Sr_{0.4}Co_{2.6}O_4$ composites

General procedure for preparation of core–shell-like $Ca(OH)_2$–$Sr_{0.4}Co_{2.6}O_4$ composite: polyethylene glycol (1 g) was dissolved in deionized water (2 mL) and followed by adding $Ca(OH)_2$ powder (1.0 g). This mixture is concentrated under reduced pressure to be a solid. $Co(NO_3)_2 \cdot 6 H_2O$ (0.53 g), glycine (0.5 g), and $Sr(NO_3)_2$ (59 mg) were dissolved in deionized water (2 mL) and followed by adding ethanol (2 mL). This solution was mixed with above solid and concentrated under reduced pressure to be dry. The solid material was sequentially calcined at 180 °C for 4 h, 280 °C for 3 h, and 800 °C for 4 h to give CaO–$Sr_{0.4}Co_{2.6}O_4$ composite. After cooled to room temperature, deionized water (2.0 mL) was added for hydrolyzation in 10 min, and then dried at 120 °C for 3 h to form $Ca(OH)_2$–15 wt% $Sr_{0.4}Co_{2.6}O_4$ composite with a core–shell structure.

2.4. Hydration–dehydration cycles under Xe-lamp irradiation

$Ca(OH)_2$–15 wt% $Sr_{0.4}Co_{2.6}O_4$ was heated under the Xe lamp for 60 min and then cooled to approximately 50 °C. Deionized water (1 mL) was then added and maintained for 10 min for hydrolyzation to completely release the heat. This process represents one cycle of the photothermal hydration–dehydration. After every five cycles, *ca* 5 mg samples were collected from the photothermal-dehydration product for TG analysis. The mass values shown by the TG data were used to calculate the dehydration conversion.

3. Results and discussion

3.1. Photothermal performance of $Sr_xCo_{3-x}O_4$ and $Ca(OH)_2$–$Sr_{0.4}Co_{2.6}O_4$ composites

Generally, OVs are thermodynamically favourable in transitional-metal oxides due to their relatively low formation energies. These multifunctional OV defects significantly modulate the electronic structure, enhance ionic conductivity, and alter magnetic properties of host materials by trapping electrons and OH^- radicals, forming oxygen-containing defect species ($\cdot O_2^-$, $\cdot O_2^{2-}$, and $\cdot OH^-$), and facilitating electron and

oxygen ion mobility.[29] Notably, OVs accelerate redox reactions by promoting $Co^{3+} \leftrightarrow Co^{2+}$ interconversion, effectively enhancing the catalytic cycle efficiency for cobalt redox processes.[30] Spinel Co_3O_4, composed of tetrahedral Co^{2+}–O and octahedral Co^{3+}–O sites, exhibits bifunctional catalytic activity for both oxygen evolution and oxygen reduction reactions.[31] Consequently, AB_2O_4-type spinel oxides with Co as the B-site cation demonstrate considerable potential for intentional OV generation and constructing oxygen-deficient redox-active frameworks. Strategic substitution of Co^{2+} ions enables precise chemical stoichiometry control over both the redox potential and OV concentrations.[32] Furthermore, introducing larger A-site cations induces possibly significant lattice expansion, resulting in enhanced OV formation and improved light absorption characteristics. Hence a series of $A_yCo_{2+x}O_4$ ($x + y = 1$) solid solutions were synthesized through a controlled nitrate pyrolysis process, demonstrating enhanced photoresponse properties. As experimentally verified, all doped variants (A = Sr^{2+}, Cu^{2+}, Zn^{2+}, and Ca^{2+}) exhibited substantially increased light absorption compared to pristine Co_3O_4, as evidenced by UV-vis diffuse reflectance spectroscopy measurements (Fig. 1a and Table 1).

Notably, all these materials exhibit comprehensive solar spectral absorption across the entire wavelength range. Particularly, the absorption of $A_yCo_{2+x}O_4$ in NIR region is significantly higher than that of Co_3O_4 (Table 1). Compared to the absorption of vis-NIR light by pristine Co_3O_4, nano $Sr_{0.4}Co_{2.6}O_4$ exhibits 1.63-fold enhancement and a broad and intense band across the entire near-infrared region. The observed enhancement in light absorption is predominantly attributed to lattice defects induced by dopant ions.[8,9] Among the investigated systems, $Sr_xCo_{3-x}O_4$ and $Cu_{0.4}Co_{2.6}O_4$ nanoparticles demonstrate
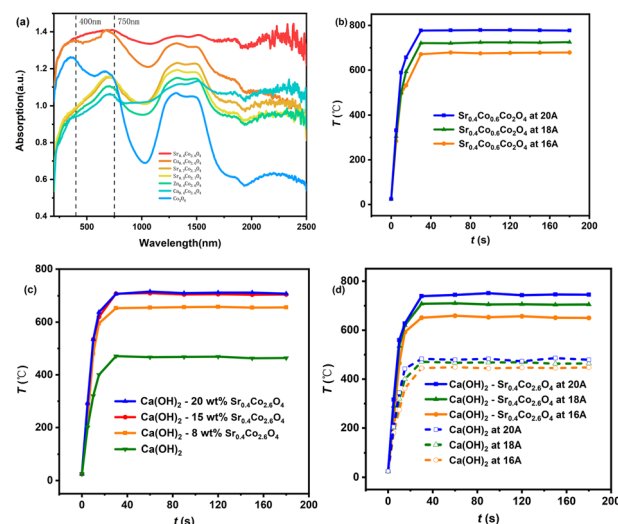
Fig. 1 (a) Absorption curves of $Sr_{0.4}Co_{2.6}O_4$, $Cu_{0.4}Co_{2.6}O_4$, and Co_3O_4. (b) Photothermal temperatures of $Sr_{0.4}Co_{2.6}O_4$ under Xe-lamp irradiation. (c) Photothermal temperatures of $Ca(OH)_2$–x-wt% $Sr_{0.4}Co_{2.6}O_4$ composites and $Ca(OH)_2$ under Xe-lamp irradiation. (d) Photothermal temperatures of $Ca(OH)_2$–15-wt% $Sr_{0.4}Co_{2.6}O_4$ and $Ca(OH)_2$ under various irradiation intensities.

Table 1 Arithmetic means of absorption in UV and vis-NIR light regions

Material	200–400 nm	401–2500 nm	750–2500 nm
$Sr_{0.4}Co_{2.6}O_4$	1.303	1.364	1.35
$Cu_{0.4}Co_{2.6}O_4$	1.299	1.212	1.16
$Sr_{0.7}Co_{2.3}O_4$	0.887	1.071	1.07
$Sr_{0.3}Co_{2.7}O_4$	0.904	1.041	1.06
$Zn_{0.4}Co_{2.6}O_4$	0.852	1.059	1.09
$Ca_{0.4}Co_{2.6}O_4$	0.868	1.007	1.06
Co_3O_4	1.211	0.839	0.75

significantly stronger absorption characteristics compared to other counterparts. This enhanced optical response may be attributed to the larger ionic radii of Sr^{2+} (1.13 Å) and Jahn–Teller active Cu^{2+} (d^9, 0.74 Å) dopants, as compared to Ca^{2+} (0.99 Å), Zn^{2+} (0.72 Å), and Co^{2+} (0.72 Å).[30] Particularly, $Sr_{0.4}Co_{2.6}O_4$ exhibits superior light absorption in the long-wavelength region, suggesting a dopant concentration-dependent effect on light harvesting efficiency. Consequently, $Sr_{0.4}Co_{2.6}O_4$ was selected for further investigation.

The photothermal performance of $Sr_{0.4}Co_{2.6}O_4$ was systematically evaluated under Xe-lamp irradiation with varying light intensities (Fig. 1b). All samples demonstrated rapid temperature elevation, reaching maximum photothermal temperatures (T_p) of 679 ± 2 °C, 725 ± 2 °C, and 779 ± 3 °C within 40 seconds under irradiation with 16 A, 18 A, and 20 A current intensities, respectively. This trend confirms a linear correlation between light intensity and T_p elevation. In contrast, control samples $Cu_{0.4}Co_{2.6}O_4$ and Co_3O_4 exhibited substantially lower T_p values of 703 ± 1.7 °C and 646 ± 2 °C under identical 18 A irradiation conditions, respectively. The photothermal conversion efficiency of $Sr_{0.4}Co_{2.6}O_4$ was measured as 86.2% (SI).

Enhanced photothermal properties of $Sr_{0.4}Co_{2.6}O_4$ prompted its strategic utilization to augment light absorption efficiency in $Ca(OH)_2$. A hierarchical core–shell architecture comprising mesoporous $Sr_{0.4}Co_{2.6}O_4$ shell and $Ca(OH)_2$ core was prepared through a two-step protocol, also demonstrating optimized light-harvesting capability.[13–15] Systematic compositional optimization was conducted through precise control of $Sr_{0.4}Co_{2.6}O_4$ content at 8, 15, and 20 wt% mass fractions, designated as CaCoSr-8, CaCoSr-15, and CaCoSr-20 respectively. Photothermal performance evaluation under Xe-lamp irradiation (18 A current) revealed distinct thermal response profiles, with all composites achieving rapid temperature elevation (~40 s) to maximum values of 656 ± 3 °C (CaCoSr-8), 706 ± 4 °C (CaCoSr-15), and 711 ± 3 °C (CaCoSr-20) (Fig. 1c). The substantially lower T_p of CaCoSr-8 suggests insufficient surface coverage at 8 wt% loading, whereas comparable T_p values between CaCoSr-15 and CaCoSr-20 indicate 15 wt% nanostructured $Sr_{0.4}Co_{2.6}O_4$ achieves nearly complete core particle encapsulation. Comparative analysis demonstrated 239 °C enhancement in photothermal temperature for CaCoSr-15 compared to pristine $Ca(OH)_2$ (467 ± 3 °C), establishing its superiority for subsequent investigation. Moreover, the consistent T_p evolution patterns observed across these composites demonstrate the

reliability of both the material preparation process and the structural integrity.

The photothermal characteristics of CaCoSr-15 were systematically investigated under multiple lamp current densities, with the corresponding temperature profiles illustrated in Fig. 2d. Notably, all thermal response curves exhibit identical temperature evolution patterns compared to their parent $Sr_{0.4}Co_{2.6}O_4$ phase (Fig. 1b), verifying the photothermal temperature dependence on radiation intensity in a quantitatively reasonable manner.

Dehydration conversion (α), a critical parameter for evaluating photothermal efficiency under irradiation, was quantified via eqn (1).[19] Sintered CaCoSr-15 specimens were subjected to programmed irradiation intervals for thermogravimetric (TG) analysis to determine mass loss percentages (m_t). Fig. 2a depicts the correlation between α and irradiation duration (t/min). Under 18 A Xe-lamp irradiation, the α values reached 86.7 wt% and 97.7 wt% after 30 min and 60 min irradiation, respectively. In contrast, the bare $Ca(OH)_2$ control exhibited comparatively negligible α values of 11.4 wt% and 20.4 wt% under identical conditions. This demonstrates a 4.8-fold enhancement in photothermal conversion efficiency for CaCoSr-15 compared to pristine $Ca(OH)_2$. The nanoscale $Sr_{0.4}Co_{2.6}O_4$ component synergistically enhances both the photothermal performance and thermal storage capacity of $Ca(OH)_2$ through a dual-mode photothermal conversion and thermal storage mechanism.

$$\alpha_t = 1 - \frac{m_t}{m_0} \tag{1}$$

$$Q_t = \alpha_t \times Q_0 \tag{2}$$

$$v_Q = \frac{Q_t}{t} \tag{3}$$

where m_t denotes the mass loss percentage of the composite material as determined by thermogravimetric (TG) analysis following t-minute irradiation, m_0 represents the initial mass loss percentage under unirradiated conditions, Q_0 indicates the maximum heat storage capacity of the $Ca(OH)_2$–$Sr_{0.4}Co_{2.6}O_4$ composite system, Q_t corresponds to the accumulated thermal energy storage at t-minute irradiation intervals, and v_Q signifies the rate parameter characterizing the thermal energy storage kinetics.
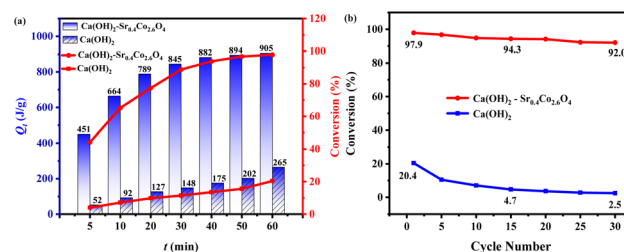

Fig. 2 (a) Relations between dehydration conversion (α) or heat amount and irradiation time (min) for $Ca(OH)_2$–15-wt% $Sr_{0.4}Co_{2.6}O_4$ and bare $Ca(OH)_2$ under irradiation. (b) Relation between dehydration-conversion and cycle number for $Ca(OH)_2$ and $Ca(OH)_2$–15-wt% $Sr_{0.4}Co_{2.6}O_4$ composite.

Table 2 Mean thermal storage rate (v_Q) at different irradiation times

	v_Q (J g^{-1} min^{-1})		
	(10 min)	(30 min)	(60 min)
Ca(OH)$_2$	8.32	4.93	4.42
CaCoSr-15	64.33	28.17	15.08

The photothermal storage capacity (Q_t) of CaCoSr-15 and Ca(OH)$_2$ under irradiation was quantified through eqn (2) and is visually presented in Fig. 2a. The composite material demonstrated a thermal storage capacity of 905 J g^{-1} after 60 min irradiation, representing a 3.4-fold enhancement compared to bare Ca(OH)$_2$. The photothermal storage rate (v_Q) was determined using eqn (3), with results tabulated in Table 2.[21,33] Pure Ca(OH)$_2$ exhibited mean v_Q values of 4.93 and 4.42 J g^{-1} min^{-1} during 30- and 60-min irradiation periods, respectively. In contrast, CaCoSr-15 achieved substantially higher rates of 28.17 J g^{-1} min^{-1} (5.7-fold increase) and 15.08 J g^{-1} min^{-1} (3.4-fold increase) under comparable conditions (Table 2). These findings collectively demonstrate that nanoscale Sr$_{0.4}$Co$_{2.6}$O$_4$ substantially enhances the photothermal storage kinetics of Ca(OH)$_2$, likely attributable to its elevated photothermal temperature profile and improved energy conversion efficiency.

3.2. Photothermal energy storage-release cycle

The limited reversibility of the pure Ca(OH)$_2$ hydration–dehydration cycle arises from restricted mass transport attributed to particle agglomeration.[34] To investigate the influence of Sr$_{0.4}$Co$_{2.6}$O$_4$ on cycle stability, a core–shell Ca(OH)$_2$–Sr$_{0.4}$Co$_{2.6}$O$_4$ composite was subjected to 60-minute irradiation under Xe-lamp illumination for energy storage. Following thermal quenching to ~50 °C, deionized water was introduced to initiate hydrolysis-driven heat release, thereby completing a full thermocyclic charge–discharge process. Post-cycling characterization involved periodic sampling (5 mg increments) of the dehydration residue every five cycles for thermogravimetric analysis. The system underwent 30 consecutive operational cycles under standardized conditions (Fig. 2b). Notably, the composite maintained exceptional structural integrity with 92.0% α retention after 30 cycles, contrasting sharply with pristine Ca(OH)$_2$'s 2.45% α preservation under identical protocols. In comparison, the analogous photothermal materials, including Mg(OH)$_2$–Co$_2$SiO$_4$–Co$_3$O$_4$,[43] Ca(OH)$_2$–CeO$_2$–Co$_3$O$_4$,[15] Mg(OH)$_2$–Co$_2$SiO$_4$–33 mol% SiO$_2$,[28] Ca(OH)$_2$–Co$_3$O$_4$–Co$_3$(PO$_4$)$_2$,[13] Ca(OH)$_2$–LaCo$_x$O$_3$ (ref. 52) and Mg(OH)$_2$–(Mn$_2$O$_3$)$_3$(Cu$_{0.6}$Mn$_{0.4}$)SiO$_3$,[33] exhibit α values of 91.5%, 91%, 92.3%, 94.4%, 89.2%, and 81.4%, respectively, after 30 cycles. This enhanced durability (37.5-fold enhancement) is attributed to the Sr$_{0.4}$Co$_{2.6}$O$_4$ shell's interconnected porous architecture, which provides superior thermal stability ($\Delta T > 300$ °C), structural robustness, and sustained mass transport pathways, thereby optimizing cycle-dependent permeability and long-term functionality.

3.3. Thermal storage kinetics of Ca(OH)$_2$–Sr$_{0.4}$Co$_{2.6}$O$_4$

To establish a reliable kinetic control equation for CaCoSr-15, a systematic evaluation of solid–gas reaction mechanism functions was conducted through comparative analysis of both differential and integral mathematical formulations (Table S1).[15,35] The dehydration mechanism of Ca(OH)$_2$ was rigorously determined to follow the contracting cylinder (R2) model, characterized by the kinetic functions $g(\alpha) = 1 - (1 - \alpha)^{1/2}$ and $f(\alpha) = 2(1 - \alpha)^{1/2}$.[19] Subsequent kinetic analysis confirmed that the R2 model constitutes the most appropriate mechanistic description for the dehydration process of the CaCoSr-15 composite system, as evidenced by statistical validation through Table S2.

The linear regression analysis of TG data for the dehydration process of CaCoSr-15 is presented in Fig. S2. The Arrhenius parameters, activation energy (E) and pre-exponential factor (A), were systematically derived from the slope and intercept of the linear regression lines, respectively. The mean kinetic parameters for CaCoSr-15 dehydration exhibited an activation energy of 166.91 ± 2.06 kJ mol^{-1} and a pre-exponential factor of 23.20 ± 0.39 (dimensionless). In contrast, bare Ca(OH)$_2$ demonstrated significantly higher kinetic barriers with $E = 198.17 ± 9.7$ kJ mol^{-1} and $\ln A = 29.40 ± 1.90$ (dimensionless).[15] The incorporation of 15 wt% Sr$_{0.4}$Co$_{2.6}$O$_4$ demonstrated remarkable enhancement in thermal storage performance, reducing the activation energy barrier by 31.3 kJ mol^{-1} (−15.8%) and decreasing $\ln A$ by 21.1%. This kinetic optimization mechanism confirms the efficacy of Sr$_{0.4}$Co$_{2.6}$O$_4$ doping in improving the dehydration kinetics of Ca(OH)$_2$ through reduced activation parameters.[19] The temperature-dependent reaction mechanisms for both Ca(OH)$_2$/Sr$_{0.4}$Co$_{2.6}$O$_4$ composite and pristine Ca(OH)$_2$ were quantitatively described using the Arrhenius-derived eqn (4) and (5), respectively.

$$\frac{d\alpha}{dT} = 1.2 \times 10^{10} \times \exp\left(-\frac{1.67 \times 10^5}{RT}\right) \times 2 \times (1 - \alpha)^{\frac{1}{2}} \quad (4)$$

$$\frac{d\alpha}{dT} = 5.8 \times 10^{12} \times \exp\left(-\frac{1.98 \times 10^5}{RT}\right) \times 2 \times (1 - \alpha)^{\frac{1}{2}} \quad (5)$$

To validate the reliability of the proposed kinetic models, the dehydration conversion (α) was determined from TGA experimental data acquired at a heating rate (β) of 2 °C min^{-1} and subsequently calculated using eqn (4) and (5). Comparative analysis presented in Fig. S3 demonstrates maximum deviations of 8.6% and 7.4% between experimental and predicted values for Ca(OH)$_2$ and CaCoSr-15 systems, respectively. These residual discrepancies fall within acceptable tolerances for thermochemical analysis, thereby confirming the validity of the kinetic parameters for reactor engineering applications and numerical simulation protocols.

3.4. X-ray photoelectron spectroscopy and oxygen-vacancy mechanism

The oxidation states of Sr and Co in the as-synthesized Sr$_{0.4}$Co$_{2.6}$O$_4$ sample were systematically investigated through

X-ray photoelectron spectroscopy (XPS) measurements. The elemental survey spectrum (Fig. S4) confirms the presence of strontium, cobalt, and oxygen in the material system. Quantitative analysis reveals that the Sr 3d core level spectrum exhibits two distinct peaks at binding energies (BE) of 134.00 eV and 135.70 eV, which are unambiguously assigned to the Sr^{2+} $3d_{5/2}$ and Sr^{2+} $3d_{3/2}$ spin–orbit components, respectively.[36] Notably, comparative analysis with the CaSrCo-15 composite demonstrates a significant downward shift ($\Delta BE > 0.8$ eV) in the Sr 3d peaks (Fig. 3a). This electronic restructuring phenomenon indicates dual interaction mechanisms: (1) strong interfacial bonding between $Ca(OH)_2$ and $SrCo_xO_4$ matrix, and (2) enhanced electron cloud density around Sr^{2+} ions resulting from electron donation via Ca–O$\cdots Sr^{2+}$ coordination bonding. Such electronic modulation effectively weakens the Ca–O bond strength through charge redistribution.[13,28]

Complementary XPS analysis of the Ca 2p region (Fig. 3b) reveals an upward binding energy shift ($\Delta BE \approx 0.6$ eV) for the $Ca(OH)_2$–$Sr_{0.4}Co_{2.6}O_4$ composite compared to pristine $Ca(OH)_2$. This electronic perturbation can be attributed to the electron-withdrawing effect induced by the $Sr_{0.4}Co_{2.6}O_4$ component. The observed electronic restructuring phenomena provide mechanistic insight into the enhanced catalytic activity of $Sr_{0.4}Co_{2.6}O_4$ and the reduced activation energy for dehydration reaction pathways (eqn (4) and (5)), as previously reported.[13,37]
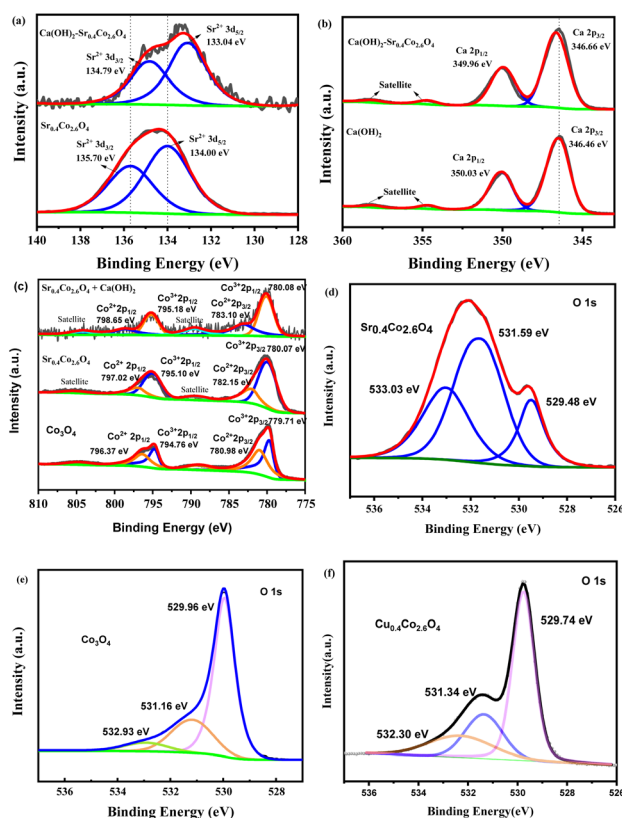

Fig. 3 X-ray photoelectron spectroscopy (XPS) spectra. (a) Deconvoluted spectrum of Sr 3d (b) Deconvoluted spectrum of Ca 2p. (c) Deconvoluted spectrum of Co 2p. (d) Deconvoluted spectrum of O 1s for $Sr_{0.4}Co_{2.6}O_4$. (e) Deconvoluted spectrum of O 1s for Co_3O_4. (f) Deconvoluted spectrum of O 1s for $Cu_{0.4}Co_{2.6}O_4$.

In the high-resolution Co 2p XPS spectrum (Fig. 3c), two primary peaks are observed at binding energies (BEs) of 780.07 and 795.10 eV, corresponding to the Co^{3+} $2p_{3/2}$ and $2p_{1/2}$ spin–orbit components in the Co–O environment, respectively. The 15.03 eV splitting between the Co $2p_{3/2}$ and Co $2p_{1/2}$ spin–orbit components is characteristic of Co^{3+} oxidation states.[38] The weaker peaks at 782.15 and 797.02 eV are assigned to the Co^{2+} $2p_{3/2}$ and $2p_{1/2}$ spin–orbit states. Additionally, satellite peaks at $\sim$789.5 and 804.84 eV are attributed to paramagnetic Co^{2+} species.[39] The peak area ratio (0.31) of Co^{2+} $2p_{3/2}$ to Co^{3+} $2p_{3/2}$ confirms their coexistence within the material, which can be formulated as $Sr_{0.4}Co_{2.6}O_4$.[39] Notably, Co^{2+} ions (d^7 electronic configuration) exhibit strong Jahn–Teller activity, promoting lattice defect formation and oxygen vacancy generation.[33] Compared to the Co^{2+} 2p BEs in Co_3O_4, the corresponding peaks in $Sr_{0.4}Co_{2.6}O_4$ exhibit a significant upshift in binding energy, indicative of electron-withdrawing effects from both Sr^{2+} doping and OVs in the nanoparticles. In contrast, the Co 2p BEs observed in the CaSrCo-15 composite exhibit a significant upward shift compared to $Sr_{0.4}Co_{2.6}O_4$ (Fig. 3c), indicative of substantial interfacial coupling between $Ca(OH)_2$ and the Co–O framework. This enhanced interaction likely facilitates dehydration through a reduction in activation energy, as delineated in the mechanistic scheme represented by eqn (4) and (5).

The deconvoluted O 1s spectra reveal three distinct binding energy peaks at 529.48, 531.59, and 533.03 eV (Fig. 3d). The primary peak at 529.48 eV corresponds to lattice oxygen species originating from Sr–O and Co–O bonding configurations. The higher-binding-energy peak at 533.03 eV is assignable to adsorbed water molecules on the material surface. Notably, the intermediate peak at 531.59 eV is attributed to OVs, which constitute 52% of the total O 1s peak area. This exceptionally high OV concentration is attributed to the substitution of Sr^{2+} ions (ionic radius = 1.13 Å) for Co^{2+} ions (ionic radius = 0.74 Å) within the crystal lattice. The substantial size disparity between these cations induces significant lattice distortion.[13,30]
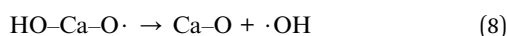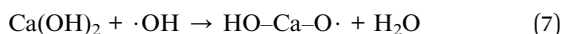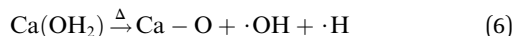
Comparative analysis demonstrates that Sr substitution induces a onefold increase in OV content relative to undoped Co_3O_4 and Cu-doped Co_3O_4 derivatives. Quantitative evaluation reveals OV populations of 25% and 28% in nano-Co_3O_4 and $Cu_{0.4}Co_{2.6}O_4$, respectively (Fig. 3e, f, S5, S6, Tables S3 and S4). The enhanced OV concentration (increased 3%) in $Cu_{0.4}Co_{2.6}O_4$ may be systematically elucidated through two synergistic mechanisms: (1) the Jahn–Teller distortion of Cu^{2+} ions (d^9 electronic configuration) that induces structural flexibility, and (2) the ionic radii proximity between Cu^{2+} (0.72 Å) and Co^{2+} cations, which effectively mitigates lattice strain during defect formation. In contrast, the considerably larger Sr^{2+} ions (1.13 Å) generate significant local strain fields, which promote OV formation via amplified metal–oxygen bond polarization.

Notably, the BE values of lattice oxygen in $Sr_{0.4}Co_{2.6}O_4$, $Cu_{0.4}Co_{2.6}O_4$, and Co_3O_4 nanoparticles were determined to be 529.48 eV, 529.74 eV, and 529.96 eV, respectively (Fig. 3d–f). This systematic increase in BE values follows an opposite trend to the OV content, suggesting that OVs exhibit electron-donor characteristics within these nanoparticle systems ($O_{OV}\cdots Co^{x+}$–$O_{lattice}$). Consequently, OVs may play a crucial role in the strong
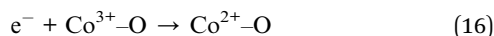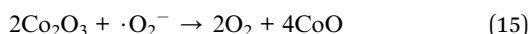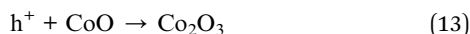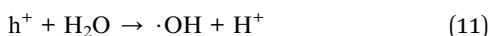
absorption of long-wavelength light (Fig. 1a and Table 1). Characterized by the presence of $\cdot O_2^-$, $\cdot O_2^{2-}$, and $\cdot OH^-$ species, OVs may also contribute to the efficient dehydration of hydroxides.[29,31]

The thermal dehydration of hydroxides proceeds through a radical-chain reaction mechanism. The process is governed by eqn (6), which constitutes the rate-determining step in the dehydration of $Ca(OH)_2$ and exhibits a comparatively elevated activation energy barrier.[40] However, this reaction mechanism shifts in the presence of hydroxyl ($\cdot OH$) and superoxide ($\cdot O_2^-$) radicals located at the OVs, where the dehydration reactions (eqn (7)–(9)) are significantly accelerated through radical-mediated pathways with reduced activation energy barriers.

$$Ca(OH_2) \xrightarrow{\Delta} Ca - O + \cdot OH + \cdot H \tag{6}$$

$$Ca(OH)_2 + \cdot OH \rightarrow HO-Ca-O\cdot + H_2O \tag{7}$$

$$HO-Ca-O\cdot \rightarrow Ca-O + \cdot OH \tag{8}$$

$$Ca(OH)_2 + \cdot O_2^- \rightarrow$$
$$HO-Ca-O^- + \cdot OOH \rightarrow CaO + H_2O + \cdot O_2^- \tag{9}$$

In addition to the photogenerated electrons and holes, OVs in $SrCo_xO_5$ can also drive various redox reactions. For instance, the photogenerated holes (h^+) residing in the valence band ($E_{VB} \approx 0.247$ eV for $Sr_2Co_2O_5$) of $Sr_xCo_{3-x}O_4$ can participate in redox reactions with adsorbed water and hydroxide species within OVs. This process facilitates hydroxyl radical generation ($\cdot OH$; $E(\cdot OH/OH^-) = 1.99$ eV vs. NHE) and promotes oxidation of superoxide radicals ($\cdot O_2^-$) and $Co^{2+}-O$ bonds to molecular oxygen (O_2; $E(O_2/\cdot O_2^-) = -0.33$ V vs. NHE) and $Co^{3+}-O$ species ($E(Co^{3+}-O/Co^{2+}-O) = 0.35$ V in $NiCo_2O_4$), respectively (eqn (10)–(13)).[29,31,32,36] Concurrently, the light-excited electrons (e^-) in the conduction band ($E_{CB} \approx -0.85$ V for $Sr_2Co_2O_5$) localized near OVs can reduce interstitial oxygen to form $\cdot O_2^-$ (eqn (14)). These redox-active species ($\cdot O_2^-$ and e^-) subsequently mediate reduction of $Co^{3+}-O$ to $Co^{2+}-O$ configurations (eqn (15) and (16)).[36]

$$h^+ + OH^- \rightarrow \cdot OH \tag{10}$$

$$h^+ + H_2O \rightarrow \cdot OH + H^+ \tag{11}$$

$$h^+ + \cdot O_2^- \rightarrow O_2 \tag{12}$$

$$h^+ + CoO \rightarrow Co_2O_3 \tag{13}$$

$$e^- + O_2 \rightarrow \cdot O_2^- \tag{14}$$

$$2Co_2O_3 + \cdot O_2^- \rightarrow 2O_2 + 4CoO \tag{15}$$

$$e^- + Co^{3+}-O \rightarrow Co^{2+}-O \tag{16}$$

The $Cu_{0.4}Co_{2.6}O_4$ system demonstrates hydroxide oxidation-driven oxygen evolution.[33] Collectively, illumination induces coupled redox cycles involving $Co^{3+}-O \leftrightarrow Co^{2+}-O$ interconversion and $O_2/\cdot O_2^-$ interplay through synergistic interactions

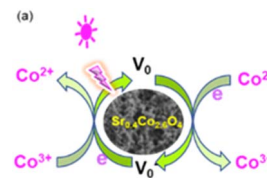**Fig. 4** (a) Redox system of oxygen vacancies and Co^{3+}/Co^{2+} within $Sr_{0.4}Co_{0.6}Co_2O_4$ nanoparticles.

between photogenerated carriers and OVs in $Sr_xCo_{3-x}O_4$ nanoparticles. This creates multiple redox processes with enhanced electron delocalization characteristics (Fig. 4a), which are characteristic of systems exhibiting metallic conductivity features.[15] Experimental validation reveals the charge carrier density (n) of $Sr_{0.4}Co_{2.6}O_4$ reaches 1.37×10^{21} cm^{-3}, comparable to quasi-metallic phases such as $WO_{2.83}$ (6.3×10^{21} cm^{-3}) and $Cu_{1.94}S$ (1×10^{21} cm^{-3}).[11,33,41,42] Thereby, a high OV density effectively reduces the bandgap,[11] enhances the concentration of photogenerated charge carriers, facilitates redox reactions, and induces pronounced localized surface plasmon resonance (LSPR) effects.

Furthermore, as demonstrated in Table 3, $Sr_{0.4}Co_{2.6}O_4$ nanoparticles exhibit the highest charge carrier density among $CeO_2-Co_3O_4$,[15] $Cr_2O_3-SiO_2$,[14] and $Co_3O_4-Co_2SiO_4$ (ref. 43) systems (SI). Experimental determination also reveals an exceptionally high charge-carrier mobility (μ) of 0.741 cm^2 V^{-1} s^{-1} for $Sr_{0.4}Co_{2.6}O_4$ nanoparticles, surpassing most reported photothermal materials (Table 3). These quantitative characteristics collectively corroborate the material's superior electrical conductivity (Table 3 and eqn (17)).[46]

$$\sigma = q \cdot n \cdot \mu \tag{17}$$

where σ is the electrical conductivity, n charge carrier density, q the charge of charge carriers, μ the mobility of charge carriers.

The Hall coefficient (R_H) of $Sr_{0.4}Co_{2.6}O_4$ was measured at -4.45×10^{-3} cm^3 C^{-1}, significantly lower than that of n-type silicon (-0.1 cm^3 C^{-1}). This negative value signifies that $Sr_{0.4}Co_{2.6}O_4$ is an n-type semiconductor, implying that the doping of Sr^{2+} ions has led to a transformation from p-type Co_3O_4. This transformation could be attributed to the high density of OV in the nanoparticles. According to eqn (18), the smallest R_H value among the corresponding materials listed in Table 3 suggests that $Sr_{0.4}Co_{2.6}O_4$ nanoparticles have the largest carrier concentration (n), which is in an agreement with the experimentally measured values.

$$R_H \propto 1/(n \times q) \tag{18}$$

where R_H is Hall coefficient, n, charge carrier density; q, the charge of charge carriers.

Comparative analysis with state-of-the-art absorber materials confirms $Sr_{0.4}Co_{2.6}O_4$'s position as the most conductive substance (163 Ω^{-1} cm^{-1}) among those documented in Table 3. This enhanced transport behaviour could be attributed to the synergetic effects of OV concentration and redox-active sites

Table 3 Light absorbers and charge carrier density, conductivity, mobility, and Hall

Materials	T (K)	Charge carrier density (cm^{-3})	Conductivity (Ω^{-1} cm^{-1})	Mobility (cm^2 V^{-1} S^{-1})	Hall (cm^3 C^{-1})
$Sr_{0.4}Co_{2.6}O_4$	340	1.37×10^{21}	163	0.741	-4.45×10^{-3}
CeO_2–Co_3O_4 (ref. 15)	340	1.12×10^{21}	113	0.630	-5.58×10^{-3}
CrO_x–SiO_2 (ref. 14)	352	1.04×10^{21}	110	0.594	-6.25×10^{-3}
Co_3O_4–Co_2SiO_4 (ref. 43)	352	1.21×10^{21}	106	0.577	-6.25×10^{-3}
Co_3O_4 (ref. 44)	773	8.26×10^{10}	10^{-4}–10^{-2} (ref. 45)	128	—

within $Sr_{0.4}Co_{2.6}O_4$, which also synergistically enhance broadband absorption across the visible and NIR spectrum (Fig. 1a).[15,45] The OV-mediated redox synergy mechanism may additionally account for the diminished light absorption observed in Co_3O_4 and $Cu_{0.4}Co_{2.6}O_4$ nanoparticles (Fig. 1a and Table 1),[41,43,47] which arises from the insufficient OV concentration and limited redox-active components within their nanostructures. Furthermore, comprehensive material characterization confirms that $Sr_{0.4}Co_{2.6}O_4$ exhibits superior photovoltaic performance compared to other listed candidates in Table 4, establishing its exceptional status as an efficient absorber.

3.5. Raman spectra

Raman spectroscopy was employed to investigate oxygen vacancy characteristics. The Raman spectrum of as-synthesized Co_3O_4 displayed four distinct vibrational modes at 651 (A1g), 615 (F2g 3), 528 (F2g 2), and 472 (Eg) cm^{-1} (Fig. 5a and S7).[53,54] The most intense band at 651 cm^{-1} corresponds to the A1g-symmetry Co^{3+}–O stretching vibration. The Eg-symmetry Co^{2+}–O stretching mode at ~190 cm^{-1} exhibited considerably weaker intensity due to signal suppression by the dominant A1g vibration mode.[54] Notably, the A1g peak of spinel Co_3O_4 serves as a structurally sensitive marker, demonstrating a significant -40 cm^{-1} blue shift relative to the stoichiometric spinel Co_3O_4 reference (691 cm^{-1}), which conclusively indicates OV formation.[55] This characteristic vibrational mode was consistently observed in Sr-doped derivatives ($Sr_xCo_{3-x}O_4$), with all compositions displaying pronounced blue shifts (Fig. 5 and Table S5).

Among these, $Sr_{0.4}Co_{2.6}O_4$ exhibited the most substantial shift (+12 cm^{-1}), surpassing the +1 cm^{-1} and +2 cm^{-1} shifts observed in $Sr_{0.3}Co_{2.7}O_4$ and $Sr_{0.7}Co_{2.3}O_4$, respectively. This enhanced blue shift correlates with increased Co–O bond strength, as evidenced by the elevated Co 2p binding energies in $Sr_{0.4}Co_{2.6}O_4$ compared to pristine Co_3O_4 (Fig. 3c). The observed bond strengthening is attributed to lattice oxygen deficiency, where greater OV concentrations induce stronger bonding interactions. The systematic correlation between blue shift magnitude and OV content indicates that $Sr_{0.4}Co_{2.6}O_4$ achieves optimal oxygen vacancy concentration among the investigated compositions.

The A1g vibrational mode of $Cu_{0.4}Co_{2.6}O_4$ exhibits a pronounced redshift, with spectral positions shifting from 651 to 642 cm^{-1}. This spectral shift suggests a weakening of Co–O bond strength induced by Cu^{2+} doping. The observed bond strength reduction is primarily ascribed to significant lattice geometric reorganization in $Cu_{0.4}Co_{2.6}O_4$, which may originate from the pronounced Jahn–Teller distortion of Cu^{2+} (d^9) ions.[33,54] This modification of metal–oxygen bonding interactions facilitates charge carrier mobility enhancement and redox reaction kinetics, thereby promoting increased charge carrier concentration and improved near-infrared light absorption efficiency, as experimentally demonstrated in Fig. 1a.[53]

3.6. Fourier transform infrared spectra

In the FTIR spectra (Fig. 5f), the absorption peaks at 1384, 661, and 565 cm^{-1} are assigned to the stretching vibrations of the Co–O bonds in spinel Co_3O_4 crystals. In comparison with

Table 4 Light absorption and free-charge-carrier density of reported materials

Material	Charge carrier density (cm^{-3})	Conductivity (Ω^{-1} cm^{-1})	Mean A^a	Reference
$(Mn_2O_3)_3CuSiO_3$	3.45×10^{21}	6.14×10^3	0.83 (FSS^b)	33
$WO_{2.83}$	6.30×10^{21}	2×10^3	–(FSS)	12 and 48
$TiO_{0.18}N_{0.86}$	2.40×10^{22}	—	-0.65 (FSS)	49
$Fe_{0.92}S_2$	1.91×10^{22}	—	–(FSS)	50
$Cu_{1.8}S$	$\sim 10^{21}$	—	0.8 (FSS)	12 and 51
$LaCoO_x$	1.30×10^{21}	163	1.12 (FSS)	52
CrO_x–SiO_2	1.04×10^{21}	110	1.46 (FSS)	14
Co_2SiO_4–SiO_2	1.20×10^{21}	108	1.27 (FSS)	28
Co_3O_4–Co_2SiO_4	1.36×10^{21}	106	1.38 (FSS)	43
Co_3O_4–$Co_3(PO_4)_2$	1.20×10^{21}	101	1.17 (FSS)	13
CeO_2–Co_3O_4	1.12×10^{21}	113	0.86 (FSS)	15
$Sr_{0.4}Co_{2.6}O_4$	1.37×10^{21}	163	1.36 (FSS)	This paper

^{a} light absorption A with mean values in visible and NIR region. ^{b} FSS, full solar spectrum.

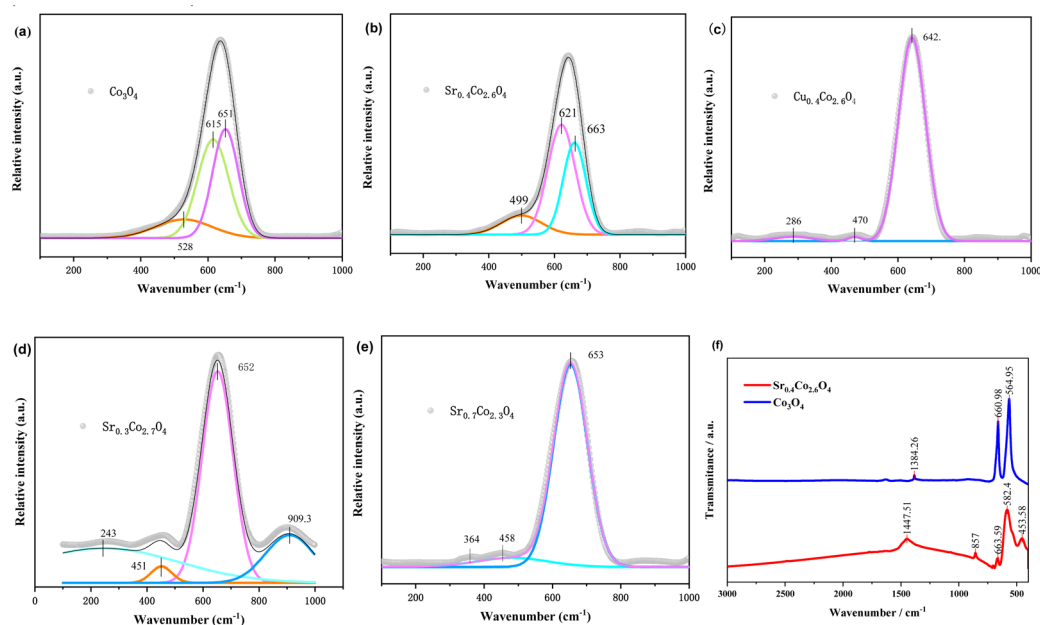**Fig. 5** (a) Raman spectroscopic characterization of as-prepared Co_3O_4. (b) Raman spectroscopic characterization of as-prepared $Sr_{0.4}Co_{2.6}O_4$. (c) Raman spectroscopic characterization of as-prepared $Cu_{0.4}Co_{2.6}O_4$. (d) Raman spectroscopic analysis of as-prepared $Sr_{0.3}Co_{2.7}O_4$. (e) Raman spectra of as-prepared $Sr_{0.7}Co_{2.3}O_4$. (f) FTIR spectra of $Sr_{0.4}Co_{2.6}O_4$ and Co_3O_4.

Co_3O_4, the corresponding absorption bands of $Sr_{0.4}Co_{2.6}O_4$ exhibit a blue shift to higher wavenumbers (1447.5, 663.6, and 582.4 cm^{-1}), indicating the strengthening of the Co–O bonds.[56] This enhancement in Co–O bond strength is consistent with the findings from both XPS and Raman spectroscopy (Fig. 3 and 5), which suggest an acceleration of oxygen migration and oxygen exchange. Moreover, these blue shifts imply the presence of OVs.[57] It has been reported that the O–O bond vibrations of $\cdot O_2^-$ result in absorption bands within the ranges of 800–1200 cm^{-1} and 400–600 cm^{-1}. The broad bands at 1447.5 and 453.6 cm^{-1} are likely generated by the superoxides (O_2^-–M^+, where M = Sr and Co) located at the OVs. The peaks at 857.0 and 453.6 cm^{-1} may be attributed to the Sr–O bonds.[57]

3.7. X-ray diffraction and microstructure

The X-ray diffraction (XRD) pattern was systematically analysed to determine the crystallographic phase composition of the synthesized $Sr_{0.4}Co_{2.6}O_4$ sample (Fig. 6a and b). The characteristic diffraction peaks observed at 2θ values of 12.89°, 18.70°, 28.58°, 32.65°, 43.96°, 58.31°, 61.80°, and 68.42° exhibited precise indexing to the (101), (110), (113), (300), (223), (330), (235), and (505) crystallographic planes of $SrCoO_x$ phase (JCPDS No. 49-0692), respectively.[58] Lattice parameter calculations derived from the XRD data revealed parameters $a = b = 9.5093$ Å, $c = 12.3893$ Å, $\alpha = \beta = 90°$, $\gamma = 120°$, and unit cell volume $V = 970.23$ Å^3. Notably, the calculated volume demonstrated a 0.65% enlargement compared to the standard $SrCoO_x$ reference value (964.2 Å^3), which could be attributed to the incorporation of Sr^{2+} ions (ionic radius 1.13 Å) substituting smaller Co^{2+} ions (0.74 Å) within the crystal lattice. This substitutional doping induced significant lattice distortion, as evidenced by

the formation of extended defects and oxygen vacancies in the nano porous framework, consistent with the complementary XPS and TEM characterizations (Fig. 3d and S8).[29] For the $Ca(OH)_2$–$Sr_{0.4}Co_{2.6}O_4$ nanocomposite system, the XRD patterns confirmed the coexistence of crystalline $Ca(OH)_2$ and $Sr_{0.4}Co_{2.6}O_4$ phases through distinct diffraction peaks corresponding to each constituent.

Additionally, energy-dispersive X-ray spectroscopy (EDS) and scanning electron microscopy (SEM) elemental mapping
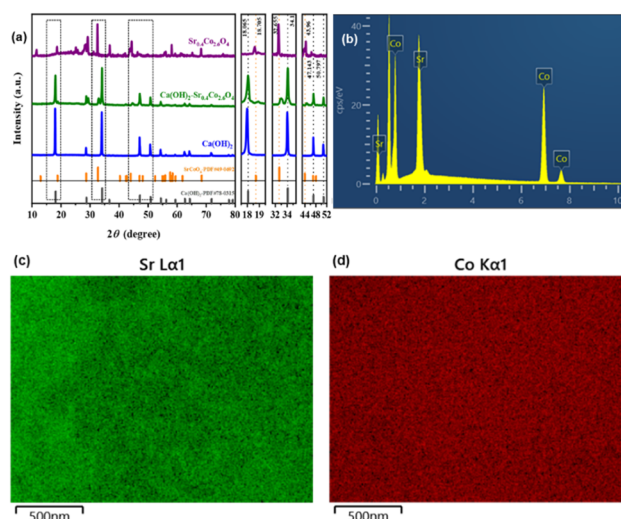

Fig. 6 (a) X-ray diffractometry (XRD) patterns of the as-prepared $Sr_{0.4}Co_{2.6}O_4$, $Ca(OH)_2$–$Sr_{0.4}Co_{2.6}O_4$, and $Ca(OH)_2$. (b) EDS results of $Sr_{0.4}Co_{2.6}O_4$ nanoparticles. (c) Elemental mapping of the SEM image of $Sr_{0.4}Co_{2.6}O_4$ nanoparticles for Sr. (d) Elemental mapping of the SEM image of $Sr_{0.4}Co_{2.6}O_4$ nanoparticles for Co.

analyses demonstrate a homogeneous distribution of Co and Sr elements within $Sr_{0.4}Co_{2.6}O_4$ nanoparticles, exhibiting atomic fractions of 87.14% and 12.86% respectively (Fig. 6b–d). These experimental values show statistical equivalence to the theoretical atomic ratio (86.7 : 13.3) of elemental composition in this compound.

Systematic characterization *via* SEM reveals the micromorphology of as-synthesized $Sr_{0.4}Co_{2.6}O_4$, featuring distinct polyhedral nanocrystalline structures coexisting with submicron-scale particles exhibiting reduced crystallinity. The material displays a well-developed porous architecture with varied pore dimensions (Fig. 7a and b).[59] This distinctive nanoarchitecture significantly enhances solar absorption capabilities while improving photothermal conversion efficiency through localized surface plasmon resonance (LSPR)-mediated thermalization mechanisms.[6,60]

The micromorphology and compositional characteristics of $Sr_{0.4}Co_{2.6}O_4$ were systematically characterized through transmission electron microscopy (TEM) and high-resolution TEM (HRTEM) analyses. The interplanar spacings of 0.206 nm, 0.249 nm, and 0.638 nm corresponded to the (223), (300), and (101) crystallographic planes of $Sr_{0.4}Co_{2.6}O_4$, respectively (Fig. 7c, d and S8). These lattice fringes demonstrated a good correspondence with the diffraction peaks at $2\theta = 32.65°$, 43.96°, and 12.89° in the X-ray diffraction spectrum (Fig. 6a, 7c and d), confirming phase consistency.

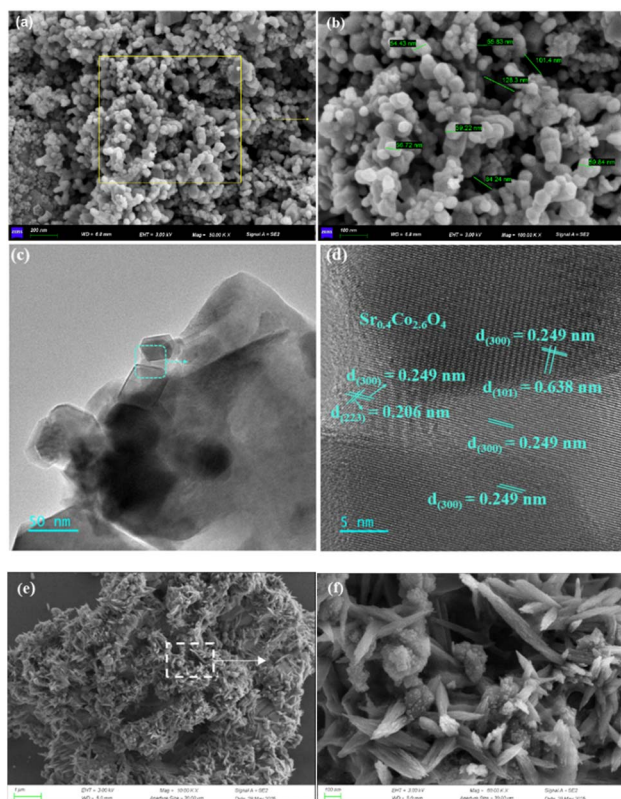The synthesized $Ca(OH)_2$–$Sr_{0.4}Co_{2.6}O_4$ composite exhibited distinctive hierarchical features as revealed by scanning electron microscopy (SEM) imaging (Fig. 7e and f). The $Sr_{0.4}Co_{2.6}O_4$ phase effectively encapsulated $Ca(OH)_2$ particles with a porous nanostructure, which could mitigate particle agglomeration during thermal energy storage/release processes.[19,21] Notably, the shell architecture contained interconnected pore networks derived from nanoparticle and nanorod assemblies, which would facilitate enhanced mass transport during charge/discharge cycles.[61] The EDS and SEM elemental mapping analyses for the $Ca(OH)_2$–$Sr_{0.4}Co_{2.6}O_4$ composite are presented in Fig. S9. These analyses clearly demonstrate a homogeneous distribution of cobalt (Co) and strontium (Sr) elements within the composite. The corresponding mass fractions are determined to be 81.65% for Co and 18.35% for Sr, as detailed in Table S6. Importantly, these experimentally obtained values exhibit excellent agreement with the theoretical mass ratio (81.40 : 18.60) of the elemental composition in this composite material.

The TEM and HRTEM images of $Ca(OH)_2$–15 wt% $Sr_{0.4}Co_{2.6}O_4$ composite further corroborate its porous architecture, the surface phase composition of $Sr_{0.4}Co_{2.6}O_4$, and the presence of numerous OVs, which are clearly delineated by circular markers (Fig. 8).

3.8. Band gaps and band energy

Furthermore, the optical band gaps (E_g) of the spinel-type absorbers were quantitatively determined through Kubelka–Munk analysis of Tauc plots, yielding values of 0.51, 0.44, 0.43, 0.40, and 0.35 eV for Co_3O_4, $Cu_{0.4}Co_{2.6}O_4$, $Sr_{0.3}Co_{2.7}O_4$, $Sr_{0.7}Co_{2.3}O_4$, and $Sr_{0.4}Co_{2.6}O_4$, respectively (Fig. 9a).[33,43] The reference Co_3O_4 nanoparticles exhibited a considerably broader band gap range of 1.76–2.17 eV, which contrasts significantly with the reduced E_g values observed in our lattice-defective Co_3O_4-based nanomaterials.[9] This systematic investigation reveals that all $A_xCo_{3-x}O_4$ compositions demonstrate substantially narrowed band gaps compared to pristine Co_3O_4. Notably, $Sr_{0.4}Co_{2.6}O_4$ displays the lowest E_g value (0.35 eV), representing a 34% reduction relative to the undoped Co_3O_4 precursor, thereby confirming the critical role of OVs in band gap engineering.

Valence band (VB) edge positions (E_{VB}) were determined through high-resolution XPS valence band spectra, revealing energy levels at 0.075, 0.43, −0.11, −0.01, and 0.54 eV for
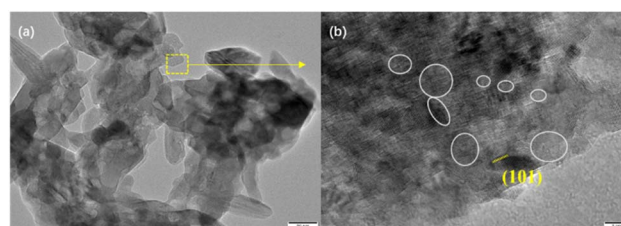
Fig. 7 (a) SEM images of the as-prepared $Sr_{0.4}Co_{2.6}O_4$. (b) Expanded image of the (a). (c) and (d) TEM and HRTEM micromorphology of the as-prepared $Sr_{0.4}Co_{2.6}O_4$. (e) SEM images of core–shell $Ca(OH)_2$–$Sr_{0.4}Co_{2.6}O_4$. (f) Expanded image of the (e).

Fig. 8 (a) TEM image of $Ca(OH)_2$–15 wt% $Sr_{0.4}Co_{2.6}O_4$ composite. (b) HRTEM image of $Ca(OH)_2$–15 wt% $Sr_{0.4}Co_{2.6}O_4$ composite with circular markers for OVs.

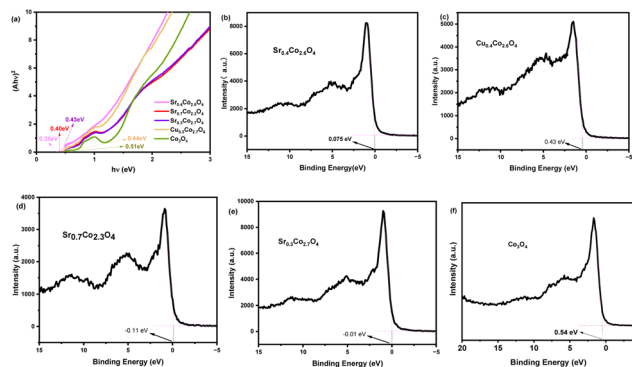**Fig. 9** (a) Tauc plots and band gaps of Co_3O_4, $Sr_xCo_{3-x}O_4$, and $Cu_{0.4}Co_{2.6}O_4$. (b) Valence-band (VB) XPS measurements of $Sr_{0.4}Co_{2.6}O_4$. (c) VB XPS pattern of $Cu_{0.4}Co_{2.6}O_4$. (d) VB XPS measurements of $Sr_{0.7}Co_{2.3}O_4$. (e) VB XPS spectra of $Sr_{0.3}Co_{2.7}O_4$. (f) VB XPS spectra of Co_3O_4.

$Sr_{0.4}Co_{2.6}O_4$, $Cu_{0.4}Co_{2.6}O_4$, $Sr_{0.7}Co_{2.3}O_4$, $Sr_{0.3}Co_{2.7}O_4$, and Co_3O_4, respectively (Fig. 9b–f). The strontium-doped derivatives exhibit considerably higher E_{VB} values than the undoped Co_3O_4, with these negative energy levels corroborating the metallic character of the materials. This elevated E_{VB}s are possibly resulted from the OVs, leading to narrowed band gaps. This electronic feature aligns with the enhanced free carrier concentration (FCC) observed in $Sr_{0.4}Co_{2.6}O_4$ through Hall effect measurements.

Conduction band (CB) positions (E_{CB}) were calculated using eqn (19), yielding respective values of −0.275, 0.03, −0.51, −0.44, and 0.03 eV for $Sr_{0.4}Co_{2.6}O_4$, $Cu_{0.4}Co_{2.6}O_4$, $Sr_{0.7}Co_{2.3}O_4$, $Sr_{0.3}Co_{2.7}O_4$, and Co_3O_4 (Fig. 10b). The comparative analysis indicates that OV formation simultaneously induces band gap narrowing and valence band elevation through two synergistic mechanisms: (1) increased free carrier density elevating the Fermi level, and (2) defect-induced electronic structure modification. These findings establish a clear correlation between OV concentration and the photothermal and optoelectronic properties critical for photothermal and photocatalytic applications.

$$E_{CB} = E_{VB} - E_g \qquad (19)$$

According to band theory, electron transfer dynamics exhibit a direct dependence on the electronic work function (Φ). The work functions of thes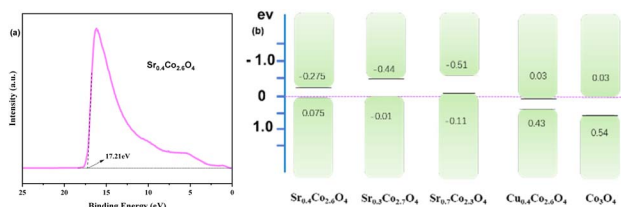e materials were investigated through ultraviolet photoelectron spectroscopy (UPS) measurements.[14,62] Experimental determination of the secondary electron cut-off energy for $Sr_{0.4}Co_{2.6}O_4$ yielded 17.21 eV (Fig. 10a). Through energy band analysis, the work function was calculated as −4.01 eV by subtracting the He I excitation energy (21.22 eV) from the secondary electron cut-off energy. This establishes the Fermi level (E_F) at 4.01 eV (where $E_F = -\Phi$), significantly below the valence band energy ($E_{VB} = 0.075$ eV) of $Sr_{0.4}Co_{2.6}O_4$ (Fig. 10b). The observed Fermi level positioning below the valence band indicates that Sr^{2+} doping induces a downward shift of the Fermi level and metallic property.[63]

This phenomenon aligns with established semiconductor physics principles, where p-type dopants exhibiting reduced Fermi levels ($E_F < E_{VB}$) demonstrate metallic conduction characteristics. Such behaviour arises from enhanced hole carrier concentration due to dopant-induced band structure modification, manifesting as increased free charge carrier density and improved electrical conductivity.[63] The experimental observations corroborate this mechanism, showing coincident high free carrier concentration (1.37×10^{21} cm^{-3}), substantial oxygen vacancy formation (52%), and elevated electrical conductivity (163 Ω^{-1} cm^{-1}, Table 3) in $Sr_{0.4}Co_{2.6}O_4$ nanoparticles.

3.9. Photocurrent intensity and photoluminescence

Photoexcitation-induced transient photocurrent responses were systematically investigated through photocurrent density measurements. Quantified photogenerated carrier densities (PCI) revealed distinct photoelectric performance among the studied cobalt oxides: Co_3O_4 exhibited 0.09 μA cm^{-2}, $Cu_{0.4}Co_{2.6}O_4$ demonstrated 0.23 μA cm^{-2}, while $Sr_{0.4}Co_{2.6}O_4$ achieved significantly enhanced photocurrent density of 1.39 μA cm^{-2} (Fig. 11a). Notably, $Sr_{0.4}Co_{2.6}O_4$ displayed a 15.4-fold photocurrent enhancement relative to pristine Co_3O_4, which may be stemmed from the narrower band gap, higher charge-carrier mobility, and n-type features. This remarkable performance enhancement is attributed to the optimized OV configuration within the Sr-doped cobalt oxide lattice, which facilitates enhanced charge transport kinetics.

Photoluminescence (PL) spectroscopy demonstrates that the PL intensity follows a descending order of $Co_3O_4 > Cu_{0.4}Co_{2.6}O_4 > Sr_{0.4}Co_{2.6}O_4$, with all exhibiting less than 1% intensity relative to SiO_2 (Fig. 11b).[14] This inverse correlation with OV content suggests that the suppressed radiative recombination rate is inversely proportional to OV concentration. The sub-1% PL

Fig. 10 (a) Ultraviolet photoelectron spectroscopy (UPS) spectra of $Sr_{0.4}Co_{2.6}O_4$. (b) Band structure of $Sr_{0.4}Co_{2.6}O_4$, $Sr_{0.3}Co_{2.7}O_4$, $Sr_{0.7}Co_{2.3}O_4$, $Cu_{0.4}Co_{2.6}O_4$, and Co_3O_4.
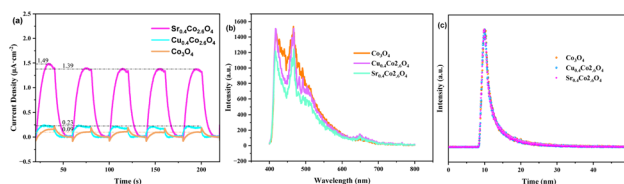
Fig. 11 (a) Photocurrent response of Co_3O_4, $Cu_{0.4}Co_{2.6}O_4$, and $Sr_{0.4}Co_{2.6}O_4$. (b) Photoluminescence spectra. (c) Photoluminescence decaying characteristics.

intensity confirms that non-radiative recombination dominates the energy relaxation pathway of photoexcited carriers, thereby enhancing photothermal conversion efficiency.[14] The highest PL intensity of the Co_3O_4 occurs in the wavelength range of 414–482 nm. The average PL intensity within this region was calculated to be 1.26 a. u. The photothermal conversion efficiency of this nano Co_3O_4 was determined to be 47.7%. For comparison, the photothermal conversion efficiency and PL intensity of Co_3O_4, $Cu_{0.4}Co_{2.6}O_4$, and $Sr_{0.4}Co_{2.6}O_4$ were determined and are summarized in Table S7. Notably, $Sr_{0.4}Co_{2.6}O_4$ exhibits the highest photothermal performance (86.2%) among these oxides.

Time-resolved photoluminescence analysis (Fig. 11c) reveals distinct carrier relaxation dynamics through two exponential components (τ_1 and τ_2), corresponding to different recombination mechanisms. The prolonged τ_2 component indicates hindered energy dissipation from excited electrons due to combined contributions from lattice defects and redox reaction.[64] This two-component decay profile provides critical insights into the competing radiative and non-radiative pathways governing carrier dynamics in these materials.

The fluorescence decay dynamics of Co_3O_4, $Cu_{0.4}Co_{2.6}O_4$, and $Sr_{0.4}Co_{2.6}O_4$ were systematically investigated through time-resolved photoluminescence (TRPL) spectroscopy, with the corresponding τ values tabulated in Table 5. The considerably shortened fluorescence τ across all samples suggest that non-radiative recombination processes predominantly govern the energy dissipation pathways of photoexcited electrons. Notably, $Sr_{0.4}Co_{2.6}O_4$ exhibits the shortest τ_2 component and average τ value alongside the weakest PL intensity, which can be attributed to synergistic quenching mechanisms involving OVs populated by paramagnetic species (O_2 and O_2^-), redox interactions between photoexcited carriers and the Co_3O_4 matrix, and its elevated photothermal temperature.[65] Intriguingly, the observed decreasing sequence of τ_2 (7.56 → 6.84 → 6.28 ns) and τ_{avg} values across Co_3O_4, $Cu_{0.4}Co_{2.6}O_4$, and $Sr_{0.4}Co_{2.6}O_4$ contrasts with the OV concentration gradient revealed by X-ray photoelectron spectroscopy (XPS) analysis (Tables S3 and S4). This paradoxical observation implies that OV introduction not only accelerates radiative decay through enhanced electron-phonon coupling but also establishes a linear correlation between OV concentration and fluorescence decay rate constant. Such behaviour contradicts conventional understanding where OV defects typically prolong radiative lifetimes.[65,66] Our findings demonstrate that OV engineering simultaneously optimizes photothermal conversion efficiency and photocurrent density by strategically modulating both PL intensity and carrier relaxation dynamics.

Conclusions

Herein, we demonstrate that the substitution of Sr^{2+} ions in $Sr_{0.4}Co_{2.6}O_4$ induces a significant concentration of oxygen vacancies (52%) and establishes a robust redox system. This structural modification notably elevates the carrier density, enabling effective light harvesting across the entire solar spectrum. The high density of oxygen vacancies, coupled with the corresponding redox activity, serves as an efficient mechanism to increase the free-charge carrier concentration (1.37×10^{21} cm^{-3}), reduce the bandgap ($E_g = 0.35$ eV), enhance NIR light absorption ($A = 1.35$), elevate photothermal conversion efficiency to be 86.2%, and amplify photocurrent generation with a 15.4-fold enhancement. These findings offer valuable insights into the mechanism of light-harvesting capabilities through oxygen-vacancy engineering. Furthermore, $Sr_{0.4}Co_{2.6}O_4$ nanoparticles substantially improve light absorption, photothermal temperature ($\Delta T = 239$ °C), and the dehydration conversion efficiency (97%) of $Ca(OH)_2$. It can also catalyse the dehydration of $Ca(OH)_2$, achieving a notable 15.8% reduction in activation energy and generating a promising candidate for one-step photothermal conversion and energy storage applications. The multifunctional $Sr_{0.4}Co_{2.6}O_4$, characterized by its high stability and remarkable structural integrity, demonstrates potential for applications in solar desalination, steam generation, photocatalysis, and photothermal reactions.

Author contributions

Lin Zhu: investigation, data curation. Rui-Min Hao: investigation, data curation. Ti-Jian Du: investigation. Cheng-Hui Liu: investigation. Zhi-Bin Xu: supervision, resources. Qin-Pei Wu: conceptualization, methodology, writing – review & editing.

Conflicts of interest

There are no conflicts to declare.

Data availability

The data supporting this article have been included as part of the supplementary information (SI). Supplementary information is available. See DOI: https://doi.org/10.1039/d5el00128e.

Notes and references

1 J. Liang, H. Liu, J. Yu, L. Zhou and J. Zhu, Plasmon-enhanced solar vapor generation, *Nanophotonics*, 2019, **8**, 771–786.

2 J. M. Zhang, B. C. Zhao, S. Z. Chen, Y. C. Wang, Y. X. Zhang, Y. F. Wang, D. S. Wei, L. P. Zhang, G. H. Rong, Y. H. Weng, J. F. Hao, B. L. Li, X. Q. Hou, X. X. Kang, Y. Zhao, F. Y. Wang, Y. X. Zhao, Y. J. Yu, Q. P. Wu, X. J. Liang and H. H. Xiao, Near-infrared light irradiation induced mild hyperthermia enhances glutathione depletion and DNA interstrand cross-link formation for efffcient chemotherapy, *ACS Nano*, 2020, **14**, 14831–14845.

Table 5 Decay time of photoluminescence

Material	τ_1/ns (rel%)	τ_2/ns (rel%)	τ_{avg}/ns
Co_3O_4	1.35 (48.9)	7.56 (51.1)	4.52
$Cu_{0.4}Co_{2.6}O_4$	1.39 (43.6)	6.84 (56.4)	4.44
$Sr_{0.4}Co_{2.6}O_4$	1.31 (42.9)	6.28 (57.1)	4.14

3 F. Zhao, Y. H. Guo, X. Y. Zhou, W. Shi and G. H. Yu, Materials for solar-powered water evaporation, *Nat. Rev. Mater.*, 2020, **5**, 388–401.

4 N. Lemcoff, N. B. Nechmad, O. Eivgi, E. Yehezkel, O. Shelonchik, R. S. Phatake, D. Yesodi, A. Vaisman, A. Biswas, N. G. Lemcoff and Y. Weizmann, Plasmonic visiblenear infrared photothermal activation of oleffn metathesis enabling photoresponsive materials, *Nat. Chem.*, 2023, 475–482.

5 P. Fu, W. Cao, T. Chen, X. Huang, T. Le, S. Zhu, D.-W. Wang, H. J. Lee and D. Zhang, Super-resolution imaging of non-ffuorescent molecules by photothermal relaxation localization microscopy, *Nat. Photonics*, 2023, **17**, 330–337.

6 X. M. Cui, Q. F. Ruan, X. L. Zhu, X. Y. Xia, J. T. Hu, R. F. Fu, Y. Li, J. F. Wang and H. X. Xu, Photothermal nanomaterials: a powerful light-to-heat converter, *Chem. Rev.*, 2023, **123**, 6891–6952.

7 M. Sayed, J. Yu, G. Liu and M. Jaroniec, Non-noble plasmonic metal-based photocatalysts, *Chem. Rev.*, 2022, **122**, 10484–10537.

8 Y. Feng, J. G. Wu, Q. G. Chi, W. L. Li, Y. Yu and W. D. Fei, Defects and aliovalent doping engineering in electroceramics, *Chem. Rev.*, 2020, **120**, 1710–1787.

9 C. L. Chen, M. Wang, X. Chen, X. C. Chen, Q. Fu and H. Deng, Recent progress in solar photothermal steam technology for water purification and energy utilization, *Chem. Eng. J.*, 2022, **448**, 137603.

10 P. Liu, X. Y. Li, L. Xu, C. Chen, B. L. Yuan, L. Labiadh, Y. B. Hu and M. L. Fu, Recent progress in interfacial photo-vapor conversion technology using metal sulfide-based semiconductor materials, *Desalination*, 2022, **527**, 115532.

11 L. Sun, Z. Li, R. Su, Y. Wang, Z. Li, B. Du, Y. Sun, P. Guan, F. Besenbacher and M. Yu, Phase-transition induced conversion into a photothermal material: quasi-metallic $WO_{2.9}$ nanorods for solar water evaporation and anticancer photothermal therapy, *Angew. Chem., Int. Ed.*, 2018, **57**, 10666–10671.

12 Y. Y. Li, Y. K. Weng, X. M. Yin, X. J. Yu, S. R. S. Kumar, N. Wehbe, H. J. Wu, H. N. Alshareef, S. J. Pennycook, M. B. H. Breese, J. S. Chen, S. Dong and T. Wu, Orthorhombic Ti_2O_3: a polymorph-dependent narrow-bandgap ferromagnetic oxide, *Adv. Funct. Mater.*, 2018, **28**, 1705657.

13 C.-H. Liu, R.-M. Hao, J. Peng, W.-X. Liu, X.-A. Ji, L. Zhu, Z.-B. Xu and Q.-P. Wu, Improved absorption of phosphates through interface junctions and photothermal–energy–storage capability of $Ca(OH)_2$–$(Co_3O_4$–$Co_3(PO_4)_2)$, *Chem. Eng. Sci.*, 2025, **304**, 120993.

14 R.-M. Hao, L. Zhu, T.-F. Shang, Z.-B. Xu and Q.-P. Wu, Strong absorption of silica over full solar spectrum boosted by interfacial junctions and light–heat–storage of $Mg(OH)_2$–$(CrO_x$–$SiO_2)$, *Chem. Eng. J.*, 2024, **497**, 154979.

15 L. Zhu, R.-M. Hao, C.-Y. Chang, Z.-B. Xu, J. Peng, C.-H. Liu, X.-A. Ji, W.-X. Liu and Q.-P. Wu, Outstanding photothermal performance of metal-like CeO_2–Co_3O_4 and excellent photothermal storage of $Ca(OH)_2$–CeO_2–Co_3O_4, *Sol. Energy*, 2024, **275**, 112616.

16 Y. H. Hu, B. Y. Zhang, F. Haque, G. H. Ren and J. Z. Ou, Plasmonic metal oxides and their biological applications, *Mater. Horiz.*, 2022, **9**, 2288–2324.

17 S. Koohi-Fayegh and M. A. Rosen, A review of energy storage types, applications and recent developments, *J. Energy Storage*, 2020, **27**, 101047.

18 R. Bravo, C. Ortiz, R. Chacartegui and D. Friedrich, Hybrid solar power plant with thermochemical energy storage: A multi-objective operational optimisation, *Energy Convers. Manage.*, 2020, **205**, 112421.

19 Y. T. Li, M. T. Li, Z. B. Xu, Z. H. Meng and Q. P. Wu, Dehydration kinetics and thermodynamics of $ZrO(NO_3)_2$-doped $Ca(OH)_2$ for chemical heat storage, *Chem. Eng. J.*, 2020, **399**, 125841.

20 C. Ortiz, J. M. Valverde, R. Chacartegui, L. A. Perez-Maqueda and P. Gimenez, The calcium-looping ($CaCO_3$/CaO) process for thermochemical energy storage in concentrating solar power plants, *Renewable Sustainable Energy Rev.*, 2019, **113**, 109252.

21 M.-T. Li, Y.-T. Li, L. Sun, Z.-B. Xu, Y. Zhao, Z.-H. Meng and Q.-P. Wu, Tremendous enhancement of heat storage efficiency for $Mg(OH)_2$-MgO-H_2O thermochemical system with addition of $Ce(NO_3)_3$ and LiOH, *Nano Energy*, 2021, **81**, 105603.

22 Y. Da, Y. Xuan, L. Teng, K. Zhang, X. Liu and Y. Ding, Calcium-based composites for direct solar-thermal conversion and thermochemical energy storage, *Chem. Eng. J.*, 2020, **382**, 122815.

23 C. Song, X. L. Liu, H. B. Zheng, C. Bao, L. Teng, Y. Da, F. Jiang, C. Li, Y. L. Li, Y. M. Xuan and Y. L. Ding, Decomposition kinetics of Al- and Fe-doped calcium carbonate particles with improved solar absorbance and cycle stability, *Chem. Eng. J.*, 2021, **406**, 126282.

24 H. B. Zheng, C. Song, C. Bao, X. L. Liu, Y. M. Xuan, Y. L. Li and Y. L. Ding, Dark calcium carbonate particles for simultaneous full-spectrum solar thermal conversion and large-capacity thermochemical energy storage, *Sol. Energy Mater. Sol. Cells*, 2020, **207**, 110364.

25 Y. Da and J. L. Zhou, Multi-doping strategy modified calcium-based materials for improving the performance of direct solar-driven calcium looping thermochemical energy storage, *Sol. Energy Mater. Sol. Cells*, 2022, **238**, 111613.

26 Y. Da, J. L. Zhou and F. D. Zeng, Calcium-based composites directly irradiated by solar spectrum for thermochemical energy storage, *Chem. Eng. J.*, 2023, **456**, 140986.

27 B. Li, Y. Li, Y. Dou, Y. Wang, J. Zhao and T. Wang, SiC/Mn co-doped CaO pellets with enhanced optical and thermal properties for calcium looping thermochemical heat storage, *Chem. Eng. J.*, 2021, **423**, 130305.

28 R.-M. Hao, L. Zhu, S.-Y. Zheng, Z.-B. Xu and Q.-P. Wu, Enhanced light absorption and photothermal efficiency of silica and silicates by heterojunctions and direct photothermal energy storage of $Mg(OH)_2$–$(Co_2SiO_4$–$SiO_2)$, *ACS Sustain. Chem. Eng.*, 2024, **12**, 12052–12063.

29 K. Y. Zhu, F. Shi, X. F. Zhu and W. S. Yang, The roles of oxygen vacancies in electrocatalytic oxygen evolution reaction, *Nano Energy*, 2020, **73**, 104761.

30 H. R. Liang, H. H. Zhu, M. Zhang, S. Y. Hou, Q. Y. Li and J. J. Yang, Oxygen vacancies promoted the generation of sulfate radicals and singlet oxygen by peroxymonosulfate activation with Co_3O_4 quantum dots/g-C_3N_4 nanosheets, *Chem. Eng. J.*, 2024, **284**, 119463.

31 Y. Wang, Y. Han, W. R. Suo, J. L. Zhang, X. Y. Lai, Z. M. Li, Z. Z. Liang and G. Z. Cao, Transition-metal oxides with peak oxygen vacancy content for oxygen electrocatalysis, *Sci. China Mater.*, 2023, **66**, 4357–4366.

32 H. Yuan, J. T. Li, W. Yang, Z. C. Zhuang, Y. Zhao, L. He, L. Xu, X. B. Liao, R. Q. Zhu and L. Q. Mai, Oxygen vacancy-determined highly efficient oxygen reduction in $NiCo_2O_4$/hollow carbon spheres, *ACS Appl. Mater. Interfaces*, 2018, **10**, 16410–16417.

33 R.-M. Hao, C.-Y. Chang, L. Zhu, Z.-B. Xu, J. Ma and Q.-P. Wu, Strong absorption of $(Mn_2O_3)_3CuSiO_3$ with Jahn–Teller elongation and direct photothermal storage of $(Mn_2O_3)_3CuSiO_3$–$Mg(OH)_2$, *Chem. Eng. Sci.*, 2024, **294**, 120080.

34 M. Xu, X. Huai and J. Cai, Agglomeration behavior of calcium hydroxide/calcium oxide as thermochemical heat storage material: a reactive molecular dynamics study, *J. Phys. Chem. C*, 2017, **121**, 3025–3033.

35 C. Huang, M. Xu and X. Huai, Experimental investigation on thermodynamic and kinetic of calcium hydroxide dehydration with hexagonal boron nitride doping for thermochemical energy storage, *Chem. Eng. Sci.*, 2019, **206**, 518–526.

36 N. Umesh, A. Sathiyan, S. F. Wang, E. Elanthamilan, J. P. Merlin and J. A. Jesila, A simple chemical approach for synthesis of $Sr_2Co_2O_5$ nanoparticles and its application in the detection of chloramphenicol and in energy storage systems, *J. Electroanal. Chem.*, 2021, **880**, 114911.

37 E.-X. Ren, D.-Y. Wang, Y.-T. Li, L. Zhu, C.-Y. Chang, L. Sun, Z.-B. Xu and Q.-P. Wu, Thermochemical energy storage drastically enhanced by zirconium oxide and lithium hydroxide for magnesium hydroxide, *Energy Storage*, 2022, **4**, e292.

38 S. B. Hammouda, F. Zhao, Z. Safaei, V. Srivastava, D. L. Ramasamy, S. Iftekhar, S. Kalliola and M. Sillanpaa, Degradation and mineralization of phenol in aqueous medium by heterogeneous monopersulfate activation on nanostructured cobalt based-perovskite catalysts $ACoO_3$ (A = La, Ba, Sr and Ce): characterization, kinetics and mechanism study, *Appl. Catal., B*, 2017, **215**, 60–73.

39 T. Y. Wu, X. Li, C. H. Weng, F. Ding, F. L. Tan and R. Y. Duan, Highly efficient $LaMO_3$ (M = Co, Fe) perovskites catalyzed Fenton's reaction for degradation of direct blue 86, *Environ. Res.*, 2023, **227**, 115756.

40 R. Priya, S. Kainth, D. Kumar, P. Sharma, P. K. Diwan and O. P. Pandey, Investigating transformation kinetics of yttrium hydroxide to yttrium oxide, *Mater. Chem. Phys.*, 2022, **287**, 126243.

41 J. M. Luther, P. K. Jain, T. Ewers and A. P. Alivisatos, Localized surface plasmon resonances arising from free carriers in doped quantum dots, *Nat. Mater.*, 2011, **10**, 361–366.

42 N. Orlovskaya, D. Steinmetz, S. Yarmolenko, D. Pai, J. Sankar and J. Goodenough, Detection of temperature- and stress-induced modifications of $LaCoO_3$ by micro-Raman spectroscopy, *Phys. Rev. B: Condens. Matter Mater. Phys.*, 2005, **72**, 014122.

43 R.-M. Hao, E.-X. Ren, W. Ran, Z.-B. Xu and Q.-P. Wu, Exceptionally boosted absorption of silicates by interfacial junctions and direct light–heat–energy storage using $Mg(OH)_2$–$(Co_2SiO_4$–$Co_3O_4)$, *Sustainable Mater. Technol.*, 2024, **42**, e01142.

44 P. Srinivasan, A. J. Kulandaisamy, G. K. Mani, K. J. Babu, K. Tsuchiya, J. Bosco and B. Rayappan, Development of an acetone sensor using nanostructured Co_3O_4 thin films for exhaled breath analysis, *RSC Adv.*, 2019, **9**, 30226–30239.

45 R. S. Desai, V. S. Jadhav, P. S. Patil and D. S. Dalavi, Recent advances in hydrothermally and solvothermally grown Co_3O_4 nanostructures for electrochemical energy storage (EES) applications: a brief review, *Mater. Adv.*, 2024, **5**, 920–960.

46 Z. Witkiewicz, K. Jasek and M. Grabka, Semiconductor gas sensors for detecting chemical warfare agents and their simulants, *Sensors*, 2023, **23**, 3272.

47 J. U. Kim, S. Lee, S. J. Kang and T.-i. Kim, Materials and design of nanostructured broadband light absorbers for advanced light-to-heat conversion, *Nanoscale*, 2018, **10**, 21555–21574.

48 Y. H. Chang, Z. G. Wang, Y. E. Shi, X. C. Ma, L. Ma, Y. Q. Zhang and J. H. Zhan, Hydrophobic $W_{18}O_{49}$ mesocrystal on hydrophilic PTFE membrane as an efficient solar steam generation device under one sun, *J. Mater. Chem. A*, 2018, **6**, 10939–10946.

49 X. Cheng, X. Bai, J. Yang, X. Zhu and J. Wang, Titanium oxynitride spheres with broad plasmon resonance for solar seawater desalination, *ACS Appl. Mater. Interfaces*, 2022, **14**, 28769–28780.

50 M. G. Gong, D. Ewing, M. Casper, A. Stramel, A. Elliot and J. Z. Wu, Controllable synthesis of monodispersed $Fe_{1-x}S_2$ nanocrystals for high-performance optoelectronic devices, *ACS Appl. Mater. Interfaces*, 2019, **11**, 19286–19293.

51 L. Chen, H. Hu, Y. Chen, J. Gao and G. Li, Plasmonic $Cu_{2-x}S$ nanoparticles: a brief introduction of optical properties and applications, *Mater. Adv.*, 2021, **2**, 907–926.

52 L. Zhu, R. M. Hao, C. Y. Chang and Q. P. Wu, Excellent absorption of $LaCo_xO_3$ over full solar spectrum and direct photothermal energy storage of $Ca(OH)_2$–$LaCo_xO_3$, *J. Sol. Energy Res. Updates*, 2023, **10**, 93–101.

53 Q. Zhang, P. Yang, H. Zhang, J. Zhao, H. Shi, Y. Huang and H. Yang, Oxygen vacancies in Co_3O_4 promote CO_2 photoreduction, *Appl. Catal., B*, 2022, **300**, 120729.

54 K. S. Kumar, L. Reddy, M. R. Hatshan, N. Roy, J. S. Kim and S. W. Joo, Comprehensive characterization of octahedral Co_3O_4 doped with Cu induces oxygen vacancies as

a battery-type redox active electrode material for supercapacitors, *Ceram. Interfaces*, 2024, **50**, 34726–34739.

55 Y. J. Sun, J. Z. Jiang, Y. Liu, S. L. Wu and J. Zou, A facile one-pot preparation of Co_3O_4/g-C_3N_4 heterojunctions with excellent electrocatalytic activity for the detection of environmental phenolic hormones, *Appl. Surf. Sci.*, 2018, **430**, 362–370.

56 S. Zhang and G. Galli, Understanding the metal-to-insulator transition in $La_{1-x}Sr_xCoO_{3-\delta}$ and its applications for neuromorphic computing, *npj Comput. Mater.*, 2020, **6**, 170.

57 H. Zhou, G. Qi, W. Li, Y. Wang and Z. Yuan, Electrolyte-gated $SrCoO_x$ FET sensor for highly sensitive detecting pH in extreme alkalinity solution, *Nano Res.*, 2024, **17**, 3079–3086.

58 G. K. Zhang, Y. Liu, X. Yang, Y. P. Wei, S. X. Ouyang and H. Liu, Comparison of synthesis methods, crystal structure and characterization of strontium cobaltite powders, *Mater. Chem. Phys.*, 2006, **99**, 88–95.

59 M. M. Natile, E. Ugel, C. Maccato and A. Glisenti, $LaCoO_3$: Effect of synthesis conditions on properties and reactivity, *Appl. Catal., B*, 2007, **72**, 351–362.

60 J. Li, W. Zhang, W. Ji, J. Wang, N. Wang, W. Wu, Q. Wu, X. Hou, W. Hu and L. Li, Near infrared photothermal conversion materials: mechanism, preparation, and photothermal cancer therapy applications, *J. Mater. Chem. B*, 2021, **9**, 7909–7926.

61 M. Hartmann, M. Thommes and W. Schwieger, Hierarchically-ordered zeolites: a critical assessment, *Adv. Mater. Interfaces*, 2021, **8**, 2001841.

62 F. Xu, K. Meng, S. Cao, C. Jiang, T. Chen, J. Xu and J. Yu, Step-by-step mechanism insights into the TiO_2/Ce_2S_3 S-scheme photocatalyst for enhanced aniline production with water as a proton source, *ACS Catal.*, 2022, **12**, 164–172.

63 P. Shyni and P. P. Pradyumnan, Fermi level tuning in modified Bi_2Te_3 system for thermoelectric applications, *RSC Adv.*, 2021, **11**, 4539–4546.

64 J. R. Lakowicz, *Principles of Fluorescence Spectroscopy*, Plenum Press, New York, 2nd edn, 1999.

65 M. L. Crespillo, J. T. Graham, F. Agullo-Lopez and Y. Zhang, Recent advances on carrier and exciton self-trapping in strontium titanate: understanding the luminescence emissions, *Crystals*, 2019, **9**, 1–16.

66 H. L. Ma, Q. Su, W. Lan and X. Q. Liu, Influence of oxygen pressure on the structure and photoluminescence of β-Ga_2O_3 nano-material prepared by thermal evaporation, *Acta Phys. Sin.*, 2008, **57**, 7322–7326.